GeoScienceWorld
Lithosphere
Volume 2024, Number 3, Article ID lithosphere_2023_160, 15 pages
https://doi.org/10.2113/2024/lithosphere_2023_160

Lithosphere

Research Article

Prediction of Overburden Failure on the Working Face Using Self-Formed Roadway Mining Technology without Coal Pillars Based on Microseismic Monitoring: A Case Study

Bosheng Hu[1,2,3] **Tong Wang**[1,2] **Panshi Xie**[1,2] **and Shenghu Luo**[2]

[1]*School of Energy and Mining Engineering, Xi'an University of Science and Technology, Xi'an, 710054, China*
[2]*Key Laboratory of Western Mines and Hazard Prevention, Ministry of Education of China, Xi'an, 710054, China*
[3]*Safty Science and Engineering, Xi'an University of Science and Technology, Xi'an, 710054, China*

Correspondence should be addressed to Tong Wang; 670298140@qq.com

Received 2 April 2023; Published 13 September 2024

Academic Editor: Enhedelihai Alex Nilot

In this study, the No.S1201-II working face of a coal mine using self-formed roadway mining technology without coal pillars was used as the engineering background, and physical experiments, numerical simulations, and field measurements were employed to study the spatiotemporal evolution laws of overburden fracture and obtain the periodic breaking law of the overburden. The results revealed the following: (1) the working face length increased after roof cutting, which led to an increase in the roadway stress on the side away from the mined area. The roof displacement remained essentially unchanged when the roadway was in the digging and cutting stages. However, the roof displacement continued to increase during the sinking and forming stages. (2) The height of the fall zone before roof cutting was approximately 17.1–19.4 m, which was 4.3–4.8 times the mining height. The maximum heights of the fracture zone on both sides and in the middle of the working face were 103.6–106.4 m and 92.4–96.1 m, respectively, corresponding to 25.9–26.6 and 23.1–24.0 times the mining height, respectively. The height of the fall zone after roof cutting was approximately 18.1 m, which was 4.5 times the mining height. The maximum heights of the fracture zone on both sides and in the middle of the working face were 100.6–105.2 m and 91.3–95.2 m, respectively, corresponding to 25.1–26.3 and 22.8–23.8 times the mining height, respectively. (3) Combined with the ground pressure behaviors and overburden breakage monitored in the field, the fracture budding phase, fracture development phase, and fracture maturation phase were divided according to the characteristics of microseismic events. A criterion for overburden deformation damage based on microseismic energy was proposed. This study provides a reference for the establishment of a microseismic-monitoring system and the application of this technology.

1. INTRODUCTION

In recent years, new technology known as self-formed roadway mining technology without coal pillars (SFRCPs) (also called the "N00" mining method) has been proposed by scholars [1, 2]. SFRCP cuts off the physical connection between the roof of the mined area and the self-formed roadway so that the roof forms a "short beam" structure, which can prevent the impact of overburden collapse on roadways [3]. After the immediate and main roofs become adjacent to the caving roadway, the collapsed gangue forms the roadway sidewall. Thus, the stress environment in the surrounding rock and the cost of roadway excavation can be optimized by eliminating coal pillars and improving roadway stability [4]. Mining technology offers significant advantages in terms of safe production and high resource recovery rate [5].

SFRCP has been explored for a long time and has been used on-site in several mines. This technology is strategically important for the global development of mining technology [2]. Many scholars have used various methods to study the support system [6], roof structure [1, 7–9],

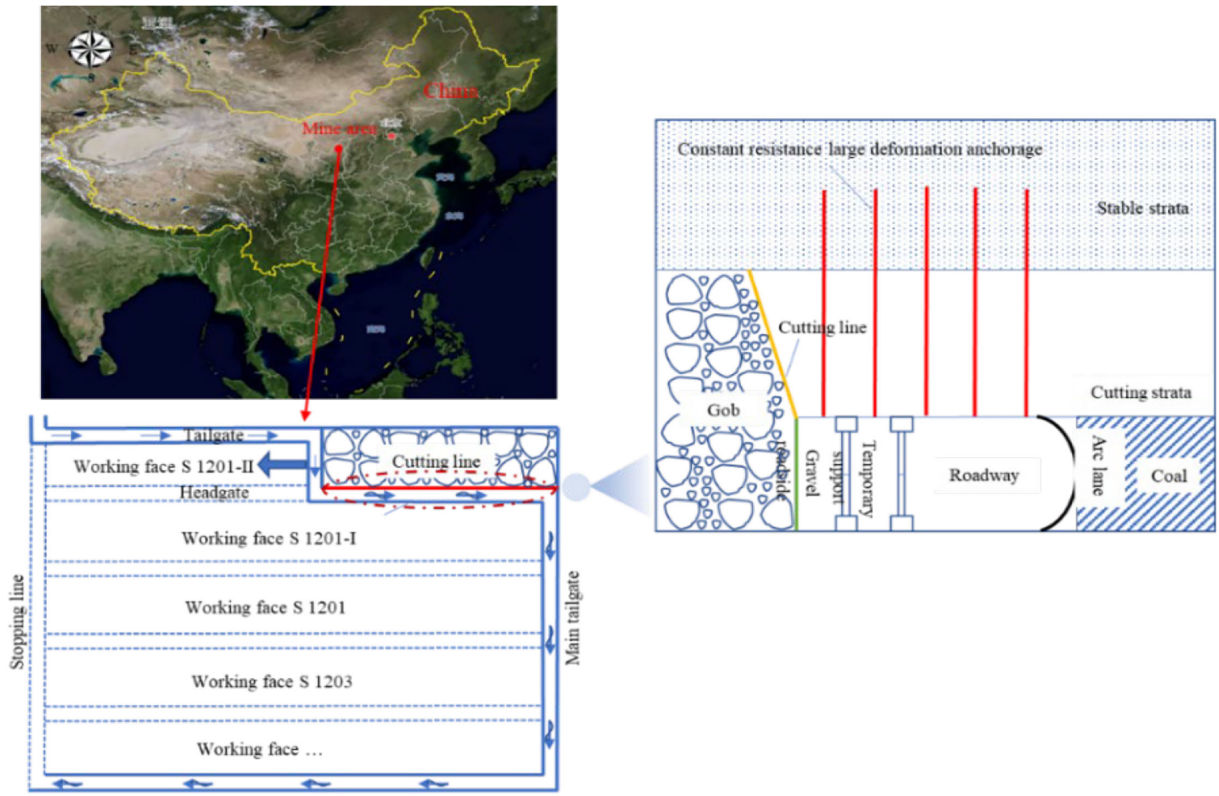

Figure 1: Schematic diagram of the working face.

roof-cutting length [10], roof stress evolution [11, 12], blasting parameters [13, 14], roadway deformation [15], and support techniques [16] for SFRCP working faces. To a certain extent, these research results have solved various engineering problems encountered in technological applications [17].

However, there are still several unresolved issues with this mining method. For example, the roof-cutting process changes the overburden integrity and stress transmission, which inevitably leads to new characteristics of the overburden movement laws under such mining conditions. As a result, the periodic weighting step and intensity of the overburden may be highly dissimilar. Moreover, it is limited by research. Most current research has been conducted from an experimental perspective, with few overburden failure investigations of high-precision field measurements. Therefore, it is necessary to conduct research on the overburden failure laws of working faces using SFRCP.

The shortcoming of traditional rock stability determination techniques is that the locations of observation points or sections are relatively scattered, making it difficult to obtain the mechanisms of stress, strain, and displacement development in a three-dimensional space [18, 19]. Usually, the selection of observation points (or sections) is based on limited engineering geological survey results. It is difficult to prevent the existence or omission of certain important geological formations, resulting in selected sections sometimes failing to respond to situations with deformed rock masses in a timely manner and endangering engineering safety [20]. Microseismic-monitoring technology has distinct advantages over traditional contact-monitoring techniques [21–24]. It monitors the release of energy events (propagated as waveforms) during rock fractures and converts wave signals into data signals using hardware and software. This enables the quantitative capture of microseismic phenomena in space, thereby characterizing the extent of rock breakage, its development trends, and stability [25, 26]. It can accurately probe the overburden damage process, thereby significantly improving the accuracy of field monitoring [27–29].

In general, the roof-cutting process for the SFRCP working face changes the overburden integrity and stress transmission, which inevitably leads to new characteristics of overburden failure under such mining conditions. Consequently, the periodic weighting step and intensity may be highly dissimilar. Therefore, this study aimed to reveal the overburden failure laws for an SFRCP working face. The No.S1201-II working face of a coal mine was used as an engineering background. Based on regional engineering geology, methods such as physical experiments, numerical simulations, and field monitoring were adopted in this study. The spatiotemporal evolution laws of overburden fractures were studied using a microseismic-monitoring system. In total, 2875 microseismic events were selected for counting and analysis. Finally, a method for predicting the overburden breakage (periodic weighting step, influence area ahead of the working face) was proposed based on the statistics of the accumulated microseismic energy in a periodic weighting step. This study provides a reference for the application of

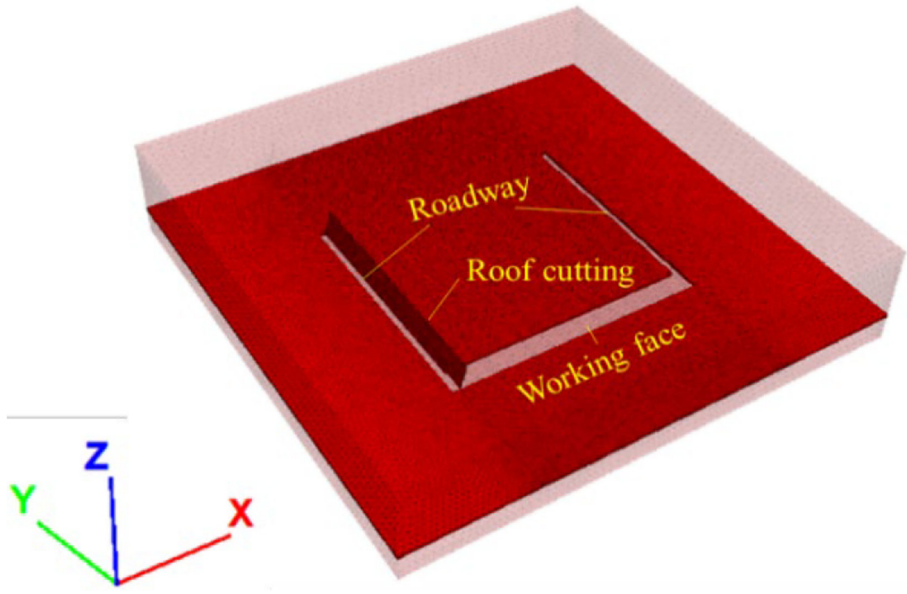

Figure 2: The numerical model.

microseismic-monitoring systems at the SFRCP working face, as well as for ground pressure prediction and control under such mining conditions.

2. CASE STUDY

The No.S1201-II working face is located north of the main west roadway in the south panel of the mine. The south of the haul roadway of this working face is approximately 120 m from the road protection coal pillar, west of the reserved No.S1201-III working face and east of the mined No.S1201-I working face. The surface of this working face is a wind-bound sandy terrain with high surface elevation in the southwest and low surface elevation in the northeast, from +1261 to +1291 m. The main mining seam of the working face is the No.2-2 coal seam, and the base elevation of the seam ranges from +1108 to +1122 m. The maximum buried depth of coal seam is 161 m. The thickness of the No.2-2 coal seam is 3.81–4.35 m, with an average thickness of 4.33 m. The thickness of the bedrock is 99.43–129.78 m, and the thickness of the weathered bedrock is 15.58–77.92 m, of which the thickness of the strongly, moderately, and weak weathered bedrock is 8.2–36.05, 7.4–31.07, and 6.11–46.35 m, respectively.

The coal mining process involves cutting coal in both directions, with a diagonal cut at the end, and two cuts in one round trip. When SFRCP is adopted, the production of a self-formed roadway behind the working face must be synchronized with coal cutting, support, and conveyor advancement. The core of this technology is reasonable roof precracking. The roof collapses under ground pressure, and the gangue is used to form the roadway sidewall, thus serving as the next working face, as shown in Figure 1. Specifically, the roof of the roadway and mined area is unbroken before cutting. There is a high degree of synergy between these two movements. The structural integrity of the roof slab decreases after cutting. The stress transfer between the roofs of the roadway and goaf is cut off at a local scale; thus, the pressure on the roof of the roadway is weakened. Consequently, the roof of the mined area slides down along the precracking surface under pressure, and the gangue becomes the roadway sidewall after the collapse.

3. NUMERICAL EXPERIMENTAL STUDY OF STRESS EVOLUTION AROUND THE WORKING FACE

During the mining process, roof cutting produce cuts off the stress transfer path. Therefore, stress evolution in the surrounding rock is more complex. As shown in this section, FLAC 3D was used to investigate the stress characteristics of the surrounding rocks during mining.

3.1. Model Setup

The numerical model is illustrated in Figure 2. The model was divided into quadrilateral meshes with 2,203,576 cells and 375,488 nodes. The length, width, and height of the model were 400, 413, and 90 m, respectively. The length of the working face was 200 m, the mining height was 4 m, and the coal pillar of the cuttings was left at 50 m. The working face was advanced in the positive direction along the y-axis, and the advance length was 200 m. In accordance with the mining process, a 15° cut was made diagonally along the haul roadway above the mined area. Displacement constraints were applied to all boundaries of the model, except for the upper boundary. The model was based on the Mohr–Coulomb failure criterion, and a large-strain deformation mode was used.

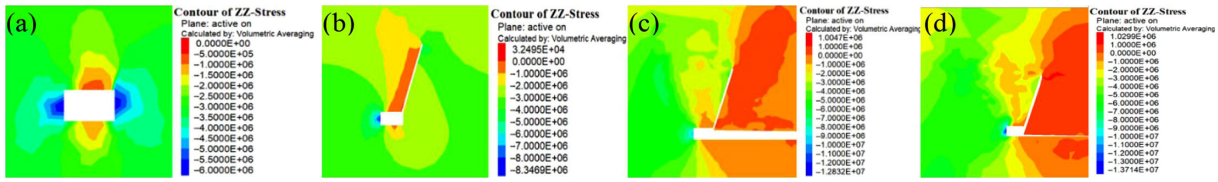

Figure 3: Stress evolution process of surrounding rock. (a) Excavation stage. (b) Cutting stage. (c) Subsidence stage. (d) Forming stage.

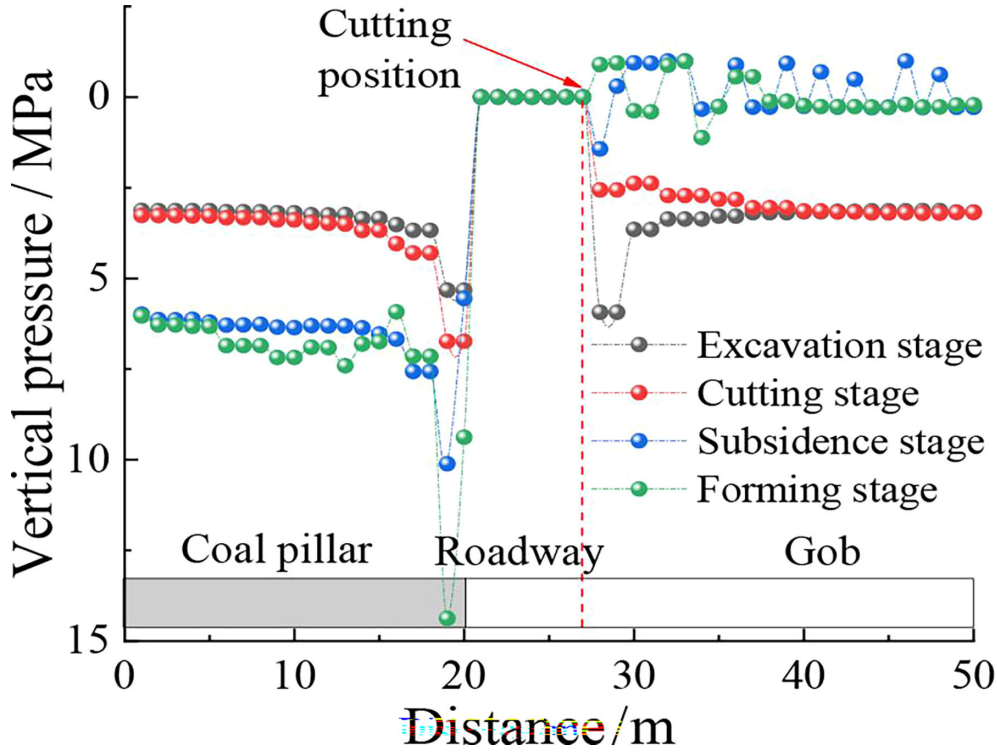

Figure 4: Stress evolution process of roadway roof.

3.2. Mechanical Parameters

The parameters adopted in the numerical model were performed comparing the results of the numerical simulation with rock mechanics tests. Specifically, uniaxial compression numerical models for various rocks were established, and the microscopic parameters were continuously adjusted to achieve a continuous approximation of the macroscopic uniaxial compressive strength and elastic modulus of the rock mass. The mechanical parameters used in the numerical calculations are listed in Table 1, considering the geological conditions of the mine and the physical and mechanical parameters of the rock.

3.3. Results

3.3.1. Stress Distribution Characteristics of the Surrounding Rock

The stress distribution pattern of the tunnel envelope during roadway excavation is shown in Figure 3(a). The stresses were concentrated on the left and right sides of the tunnel, with a maximum vertical stress of 6.19 MPa, and were relieved on the roof and floor of the tunnel, with a maximum vertical stress of 0.5 MPa. The stress distribution pattern of the roadway envelope during the roadway cutting stage is shown in Figure 3(b). The left side of the roadway had a stress concentration with a maximum vertical stress of 8.34 MPa, whereas the right side of the roadway had a weaker stress concentration owing to the presence of a slit fissure. The maximum vertical stress was 0.8 MPa. During the mining process, the roof began to sink slowly. The stress distribution pattern of the surrounding rock is shown in Figure 3(c). As shown, a large-scale stress release phenomenon occurred on the working face roof. To the left of the roadway, the phenomenon of stress concentration in the surrounding rock was more evident, and the maximum vertical stress increased to 9.32 MPa. The area of stress release on the floor increased further, similar to the degree of release.

The stress distribution pattern of the surrounding rock during the roof-cutting stage is shown in Figure 3(d). The roof then sank further into contact with the floor. The cut-down roof formed the right side of the roadway. The area and extent of stress release of the roof further increased, with the tensile stress increasing to 1.03 MPa,

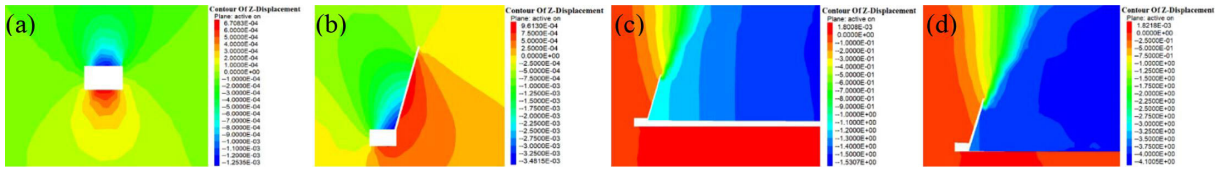

Figure 5: Displacement evolution process of surrounding rock. (a) Excavation stage. (b) Cutting stage. (c) Subsidence stage. (d) Forming stage.

Table 1: Mechanical parameters of coal and rock used in numerical simulations.

Lithologies	Density (kg/m^3)	Bulk modules (MPa)	Shear modules (MPa)	Tensile strength (MPa)	Cohesion (MPa)	Internal friction angle (°)
Fine sandstone	2,420	4,167	2,869	1.8	3.5	37
Medium sandstone	2,550	3,435	3,876	1.9	3.9	37.5
Coal	1,350	2,381	1,163	0.6	1.3	32.9
Siltstone	2,530	3,372	3,816	1.7	4.5	20.4
Fine sandstone	2,640	9,302	9,137	2.1	4.2	28

and stress concentration occurred on the left side of the roadway, with the maximum vertical stress increasing to 12.92 MPa.

The evolution of vertical stresses on the roof of the roadway is shown in Figure 4. The vertical stresses on the left wall of the roadway were 5.33, 6.74, 10.11, and 14.38 MPa when the roadway was in the excavation, cutting, sinking, and forming stages, respectively, with increases of 26.45%, 50%, and 42.24%. All the peak locations were 1 m from the left side of the roadway. The vertical stresses on the right wall of the roadway were 5.93, 2.56, 1.43, and 0.38 MPa, with increases of −56.83%, −44.14%, and −73.43%. The vertical stress on the left wall of the roadway showed an evolutionary increasing trend, and the increase was greatest after the completion of the cuttings. This indicates that the span of the working face increased after the cutting process, and the tendency to support the pressure also increased. On the right wall of the roadway, the vertical stresses increased, and the significant sinking of the roof led to a significant release of vertical stresses, with the greatest decrease occurring in the cutting stage.

3.3.2. Displacement Evolution of the Surrounding rock

The roadway displacement during the excavation stage is shown in Figure 5(a). Smaller deformations occurred on the roof, with a maximum vertical displacement of 0.001 m. The maximum floor displacement was 0.0006 m. The roadway displacement in the roof-cutting phase is shown in Figure 5(b). The maximum vertical displacement was 0.003 m at the cutting position. This was a slight increase compared to the excavation stage. The roadway displacement during mining is shown in Figure 5(c). The roof displacement further increased, with a maximum value of 1.53 m on the wall adjacent to the mined area. The displacement at the self-formation stage of the roadway is shown in Figure 5(d). The roof sank further into contact the floor, and the maximum vertical displacement of the roof was 4.1 m.

The displacement evolution process of the roadway roof is shown in Figure 6. The displacement of the roof remained largely unchanged when the roadway was in the excavation and cutting stages. During the mining and roadway self-formation stages, the displacement of the roof increased to some extent. The values for the roof above the roadway were 0.28 and 0.84 m, respectively, with the latter exhibiting an increase of 200% over the former. The peak displacements were located at the cuttings.

4. PHYSICAL EXPERIMENT FOR FRACTURE DEVELOPMENT IN THE QUARRIED OVERBURDEN

To investigate the deformation and damage characteristics of the surrounding rock during SFRCP mining, physical experiments were performed to determine the deformation and breakage characteristics of the overburden and reveal the spatial and temporal evolution of the mine pressure during the mining process.

4.1. Physical Model and Similar Material Composition

A plane-strain model was constructed for this experiment based on coal seam conditions. The geometric similarity ratio of the model was 1:120, from which the other similarity constants were derived. The similar materials selected for the model were sand and coal ash as aggregates, gypsum and white powder as cementing materials, and mica flakes as materials for the laminated strata. The composition scheme of the different materials was determined according to the similarity criterion (Table 2). The complete physical model is shown in Figure 7(a).

4.2. Results

The results of the physical experiment showed that when the working face of the No.2-2 coal seam advanced to

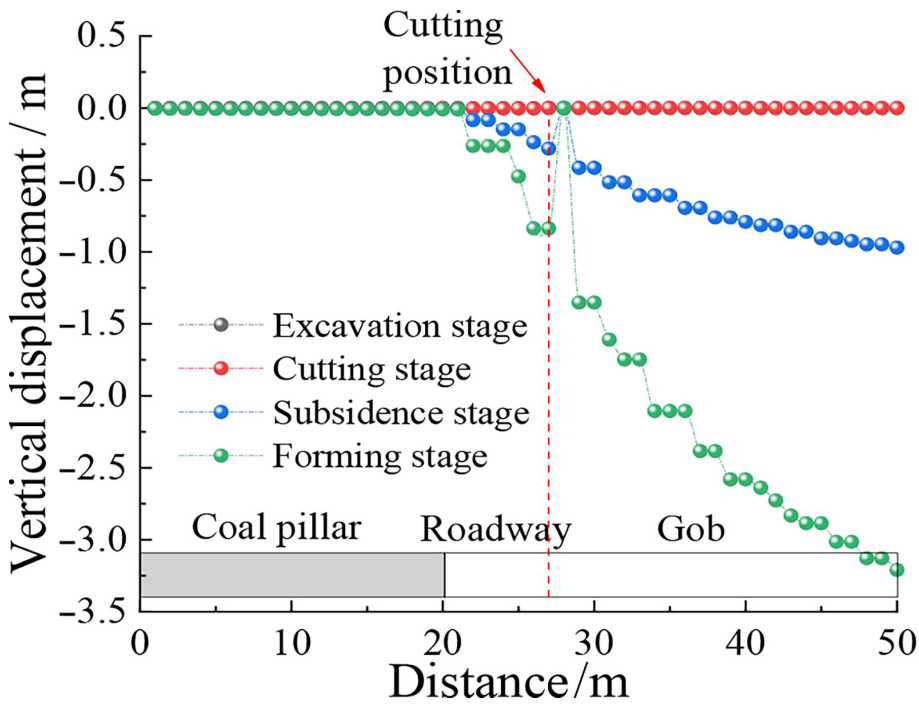

Figure 6: Displacement evolution process of the roadway roof.

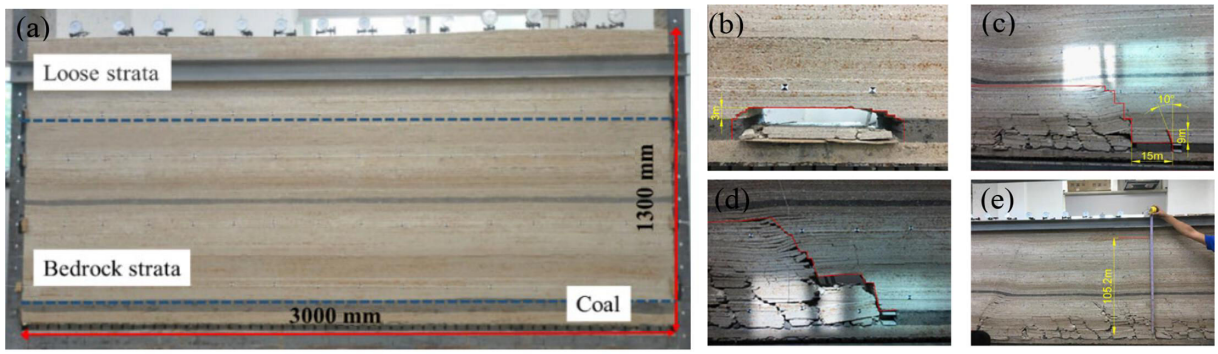

a

Figure 7: Breakage evolution law of overlying rock. (a) Experimental model. (b) Initial breakage. (c) Roof cutting and self-formed roadways. (d) Overlying breakage after roof cutting. (e) Final collapse.

39.6 m, an initial breakage occurred at 3 m of the roof and collapse occurred (Figures 7(b)–7(d)). The self-formed roadway started 15 m ahead when the working face advanced 202.2 m. Specifically, the cutting height was 9 m, and the angle was 10°. Before the cutting, the fracture zone in the middle of the working face was 95.5–96.1 m, and the ratio of fracture zone to mining height (FM ratio) was 23.8–24.0. The strata above the mined area bent further as the working face advanced, and the fissure zone tended to stabilize. The fracture development height at the edge of the working face was 105.9–106.4 m, and the FM ratio was 26.4–26.6.

The overlying rock layer reached full mining when the working face advanced to 230 m. The final development height of the fissure zone on both sides of the working face was approximately 104.3–105.2 m, and the FM ratio was 26.1–26.3. The fissure zone in the middle of the working face was 94.3–95.2 m, and the FM ratio was 23.6–23.8 owing to the continuous compaction of the overlying rock layer.

The maximum height of the fracture zone on both sides of the working face was 103.6–106.4 m, with an FM ratio of 25.9–26.6. The height of the fracture zone in the middle of the working face was 92.4–96.1 m, with a ratio of 23.1–24.0. The maximum height of the fissure zone on both sides of the working face was approximately 100.6–105.2 m, with a ratio of 25.1–26.3. The height of the fissure zone in the middle of the working face was 91.3–95.2 m, with a ratio of 22.8–23.8. In general, the height of fracture development remained essentially unchanged before and after roof cutting in different areas and even slightly decreased in

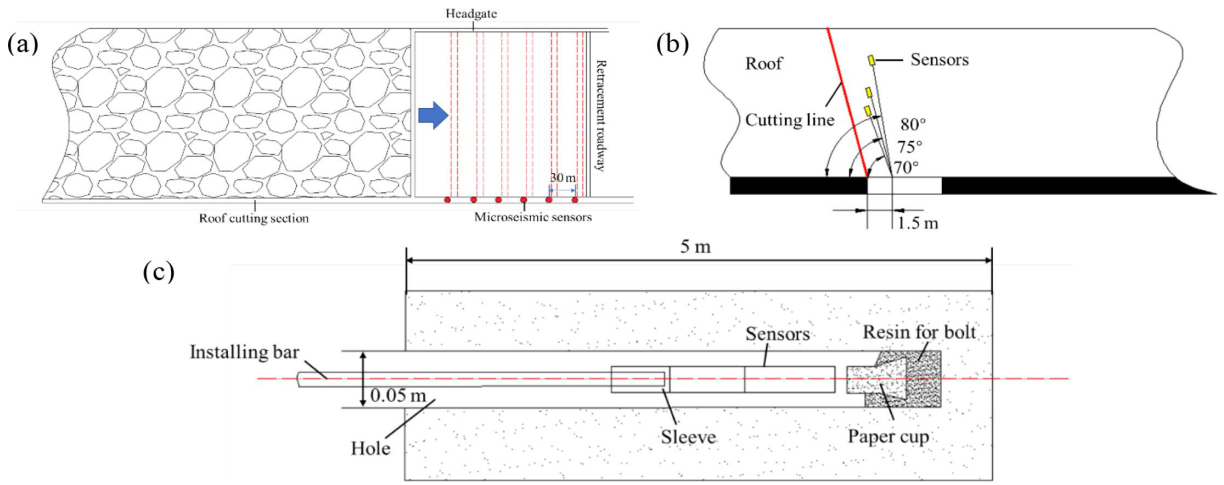

FIGURE 8: Schematic layout of microseismic-monitoring points. (a) Top view. (b) Section along the working face length. (c) Microseismic sensor installation.

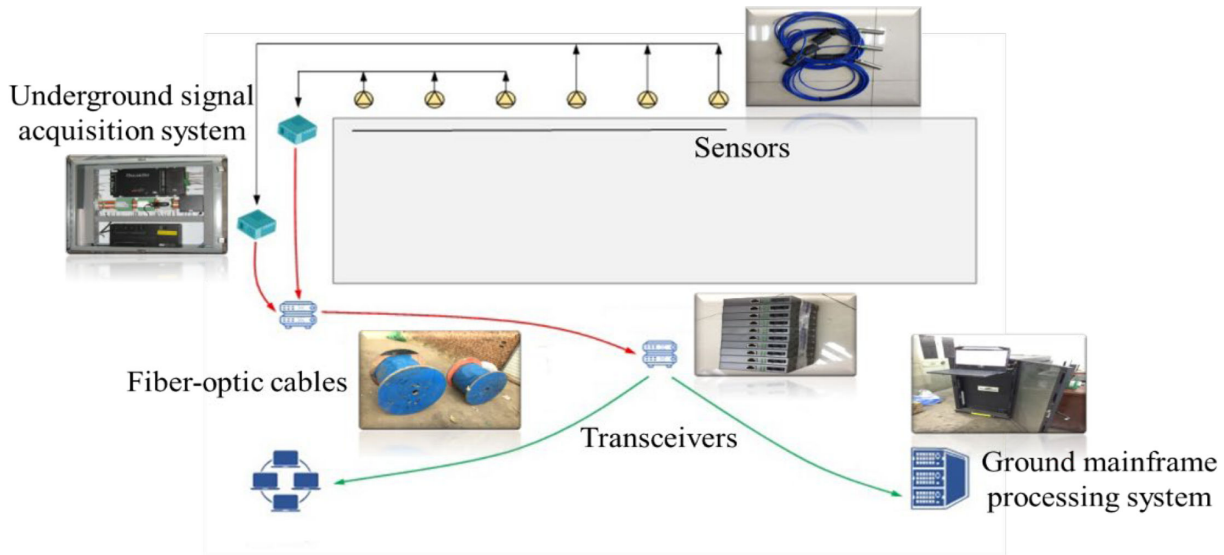

FIGURE 9: Layout of the microseismic-monitoring system.

local areas. This indicates that the roof-cutting process can improve the mechanics of the overlying rock to some extent.

5. MICROSEISMIC MONITORING AND ITS VALIDATION

A distinctive feature of microseismic-monitoring technology is that it allows for the real-time monitoring of rock properties in three dimensions. Through the acquisition and analysis of microseismic waves, the location of rock ruptures, magnitude, energy release, and nonlinear strains in the rock mass accompanied by microseismic events can be determined. Therefore, combined with the results of the physical experiments and numerical simulations in the previous section, a microseismic-monitoring system was arranged at the working face for real-time monitoring of the spatiotemporal evolution characteristics of overburden deformation under the SFRCP.

5.1. Microseismic-Monitoring Principles and System Construction

When a microseismic event occurs in the overlying strata, the spatial coordinates of the source are (x, y, z), the moment of occurrence is t, the coordinates of the ith sensor are (x_i, y_i, z_i), the moment detected by the sensor is t_i, and the average speed of acoustic wave propagation is v. Then, the equation for travel time between the source and the ith sensor is

$$(x_i - x)^2 + (y_i - y)^2 + (z_i - z)^2 = v^2(t_i - t)^2 \quad (1)$$
$$,(i = 1,, 2, \ldots, m)$$

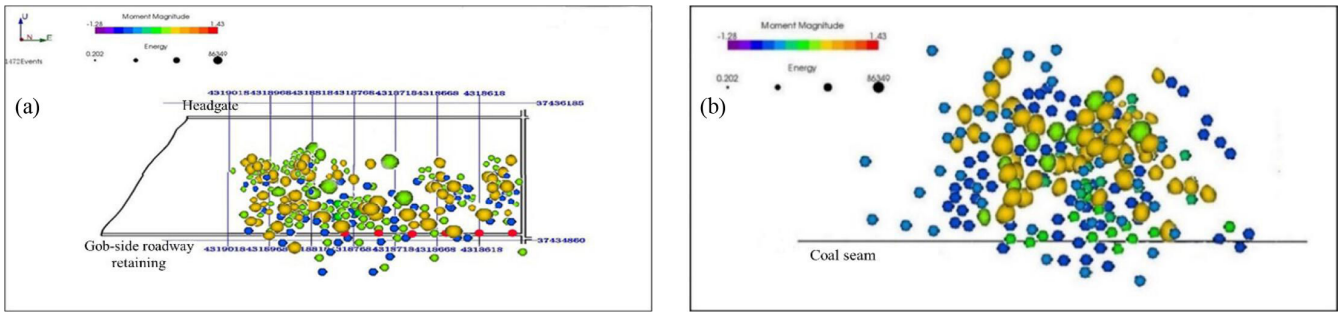

FIGURE 10: Distribution of microseismic events. (a) Top view. (b) Microseismic event distribution along the working face strike.

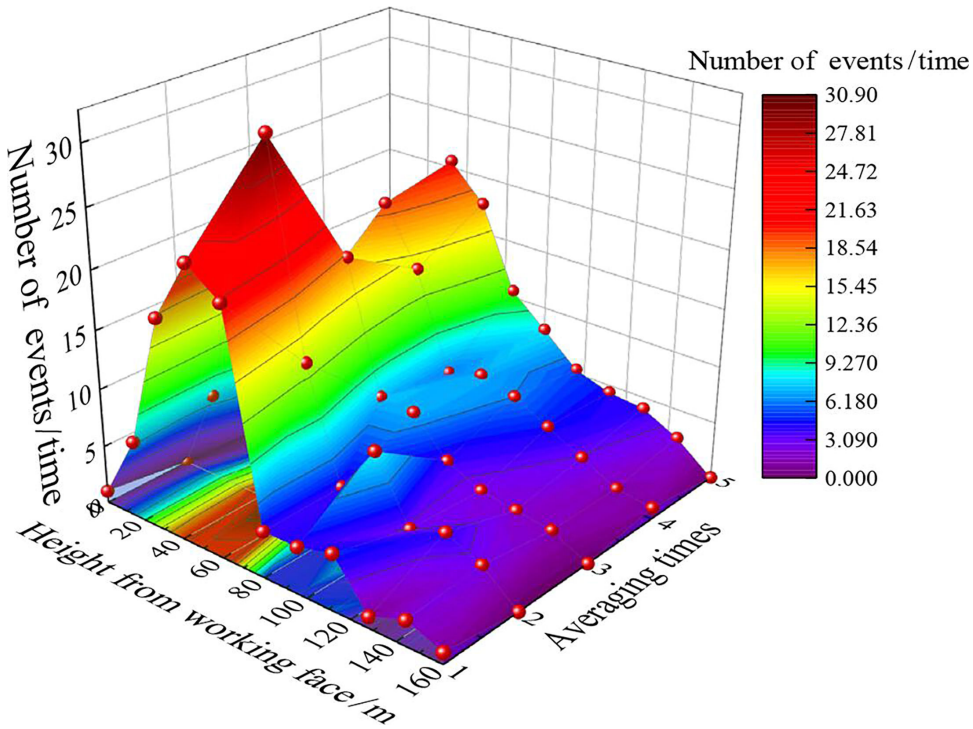

FIGURE 11: Distribution of microseismic events with vertical height.

where m is the number of sensors receiving the signal, and (x, y, z, t) is the spatiotemporal parameter of a microseismic event. This equation is difficult to solve directly because it is a nonlinear system. Therefore, it is necessary to develop a linear system to replace it. A linear system is obtained by subtracting the equation for the kth monitoring point from that for the ith monitoring point.

$$\begin{aligned} &2(x_i - x_k)x + 2(y_i - y_k)y + 2(z_i - z_k)z - 2v^2(t_i - t_k)t \\ &= x_{i2} - x_{k2} + y_{i2} - y_{k2} + z_{i2} - z_{k2} - v^2(t_{i2} - t_{k2}), (i, k = 1, 2, \cdots, m) \end{aligned} \tag{2}$$

$m(m - 1)/2$ linear equations can be produced through different combinations of i and k, of which only $m - 1$ are linearly independent. There must be more than four independent equations if a system of independent equations is to be solved. In other words, at least four sensors are required to receive the same signal.

$$d_i = V_p \times T_i \tag{3}$$

$$\triangle d_{0i} = \sqrt{(x - x_i)^2 - (y - y_i)^2 - (z - z_i)^2} \tag{4}$$

$$d_i = d_0 + \triangle d_{0i} \tag{5}$$

It is clear from the geometric relationships that three fixed points are required to locate the coordinate position (x, y, z) of a point in space, that is, three sensors are required to receive the same microrupture signal when locating a microearthquake event.

In this study, microseismic sensors were arranged based on positioning principles, as shown in Figures 8(a) and 8(b).

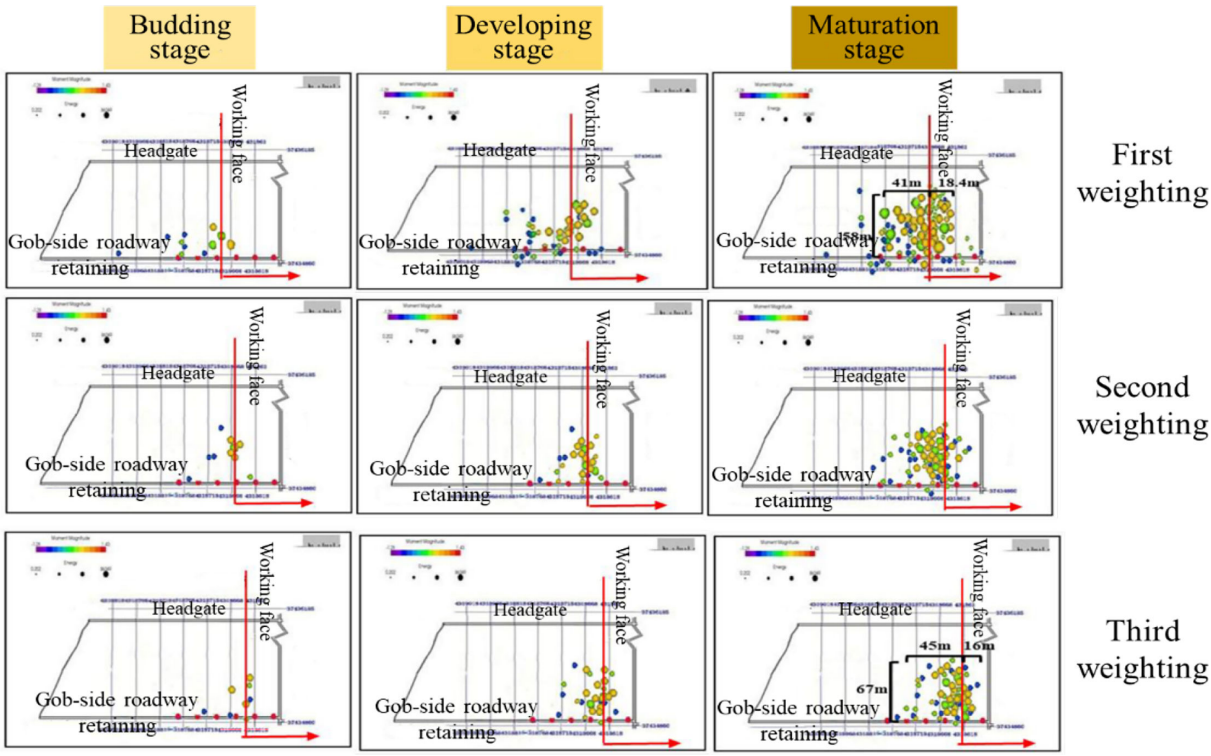

Figure 12: Top view of microseismic events during periodic pressure.

Table 2: Proportion scheme of similar materials.

Lithologies	Thickness /cm	Materials (kg/cm)			
		Sand	Gypsum	White powder	Coal ash
Fine sandstone	6	8.40	0.48	0.72	
Sandy mudstone	2	8.64	0.29	0.67	
Fine sandstone	8	8.40	0.48	0.72	
Kern stone	2	8.64	0.29	0.67	
Siltstone	16	8.53	0.21	0.86	
Kern stone	14	8.64	0.29	0.67	
Fine sandstone	6	8.40	0.48	0.72	
No.1-2 upper coal seam	3	1.96	0.10	0.49	1.96
Siltstone	11	8.53	0.21	0.86	
Fine sandstone	9	8.40	0.48	0.72	
Kern stone	19	8.64	0.29	0.67	
No.2-2 coal seam	4	1.96	0.10	0.49	1.96
Siltstone	16	8.53	0.21	0.86	

Microseismic sensors were installed at 30-m intervals in the normal section, while six sensors were installed at the same distance in the self-formed roadway section. The six sensors were divided into three layers in the vertical direction. Using this approach, a more balanced spatial distribution was formed in the overlying strata. With respect to the relevant working face, the sensors should be arranged within a relatively stable layer. They should also be able to work steadily during the mining process, thus enabling the effective monitoring of microseismic events.

There was a large amount of water and cinder inside the borehole owing to the geological conditions of the site. Only approximately 80% of cinder and water can be removed by cleaning a borehole using a special drilling machine. Consequently, it often results in the anchor debonding firmly to the rock, and sensor installation fails when traditional installation methods are used. The first step was to use the installation tool to bring the sensor to the bottom of the borehole and secure it to the rock wall. Second, the borehole was slowly filled with an appropriate amount of cement mortar to cover the sensor. Third, the hole was sealed by injecting more cement mortar. Care must be taken to prevent damage to the cables connecting the sensors during sealing. The sensor was then tested after the hole was sealed.

The monitoring system mainly consisted of sensors, an underground signal acquisition system, a ground mainframe processing system, transceivers, cable wires, fiber-optic cables, and junction boxes (Figure 9). The ground mainframe was placed in the fleet office at the wellhead, and the signal acquisition system was transported to the S1201-II retraction air window by a rubber wheelbarrow. The wiring of the monitoring system consisted of two parts: a power line and a communication line. The power line was primarily responsible for supplying power to the equipment. A network cable was used to connect the wellhead switch to

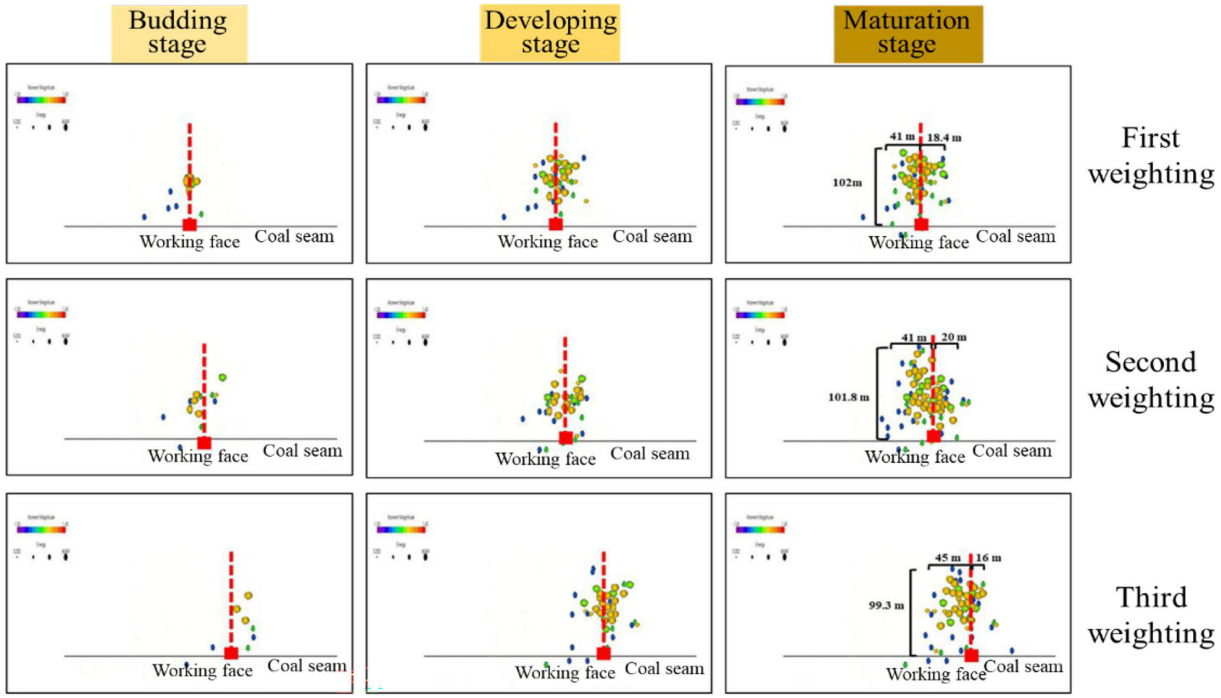

Figure 13: Sectional view of microseismic events under periodic pressure.

the ground mainframe processing system after the collector was connected to the underground signal acquisition system. Equipment such as hydraulic supports can easily damage the sensor wires as the working face advances.

Therefore, two cable-protection measures were adopted owing to the need to monitor microseismic events in the overburden above the self-formed roadway. First, the cables were protected by sleeving. The material chosen for the sleeving was a 2.0-MPa PPR pipe with a thickness of 3.5 mm, which was reinforced with a two-way junction between the pipe and the cable. Second, the cable was hung in the cable trench and tied. The microseismic-monitoring system is shown in Figure 9.

5.2. Microseismic-Monitoring Results

5.2.1. Spatiotemporal Characteristics of Microseismic Events

The microseismic-monitoring system began operating after installation of the system was completed. Until the mining of the No.S1201-II working face was finished, microseismic events between an elevation of 1285 m and a strike length of 180 m were selected. In total, 2875 microruptures were counted during the monitoring process. The distribution characteristics of the microseismic events are shown in Figure 10(b). The sphere represents a microrupture event in the overburden of the test workings, the sphere size indicates the energy level, and the color indicates the magnitude of the moment. Yellow indicates the maximum moment magnitude.

The breaking evolution characteristics of the overburden can be derived by analyzing the microseismic events during the mining process (Figure 10(b)). High-energy microseismic events were concentrated in the range 21–84 m above the coal seam. Combined with the comprehensive column diagram of the coal seam, it can be seen that many high-energy microseismic events were distributed in the medium-grained sandstone (thickness of 16.20 m), siltstone (thickness of 3.79 m), and siltstone (thickness of 30.65 m) above the coal seam. This area lay between the subcritical and main critical layers, with a high degree of fracture development. The highest number of microseismic events occurred 101.8 m vertically above the coal seam, and fewer microseismic events were distributed in the strongly weathered bedrock layer.

The farthest microseismic events occurred in the direction of the working face advancement 54–66 m from the self-formed roadway section. The microseismic events were concentrated from 31–45 m behind the coal wall to 15–24 m in front of the coal wall. The distance between the microseismic events ahead of the coal wall decreased from the lower layer to the upper layer. The maximum distance was 26 m.

The distribution of microseismic events with respect to vertical height is shown in Figure 11. With increasing height, microseismic events exhibited a trend of increasing and then decreasing. The number of microseismic events continued increasing in the range 0–48 m above the coal seam and decreasing in the range 48–160 m above the coal seam. Many microseismic events occurred at 48, 48, 48, 32, and 32 m above the coal seam, with 23, 30, 18, 19, and 20 events, respectively. The microseismic events were heavily clustered in the range 20–85 m above the coal seam and had an overall normal distribution pattern with height.

5.2.2. Periodic Characteristics of Microseismic Events

Along the direction of the working face strike, a few microseismic events were initially concentrated 23–32 m

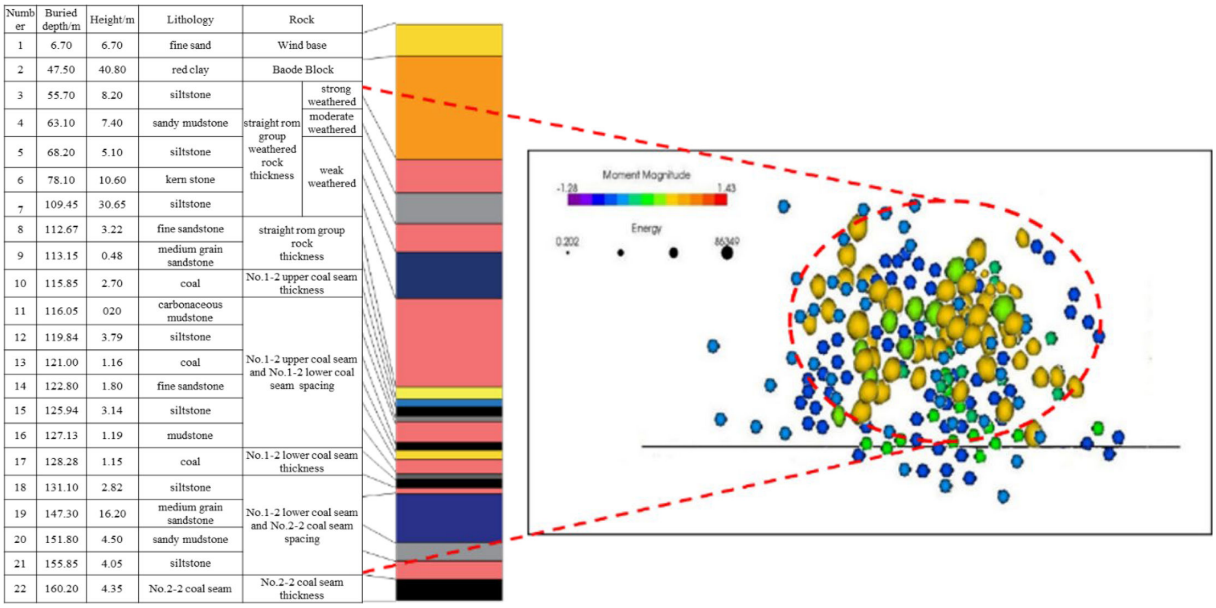

Figure 14: Distribution of the fracture zone against the comprehensive geological column map.

above the coal seam, as shown in Figure 12. The number of microseismic events increased 21–75 m above the coal seam as the face continued to advance. Many high-energy microseismic events were concentrated in the range 19.7–86 m when the working face was advanced to a certain distance.

In the direction of the working face length, the initial microseismic event distribution range went as far as 24.6 m from the self-formed roadway section. The microrupture events occurred from 23 m behind the workings to 15 m in front of them. As the working face continued to advance, the width and length of the microruptures gradually increased. The farthest distance from the microseismic event was 34 m from the self-formed roadway section. The width and length of the microrupture distribution also reached their maximum values when the working face was advanced by a certain distance. The farthest distance from the section was 67 m. The microrupture events occurred from 45 m behind the working face to 9.4 m ahead.

In summary, high-energy microseismic events occurred first in the sandstone rock above the coal seam. Subsequently, crack development continued from the lower layer to the upper layer. Microseismic events also exhibited a certain trend in the direction of the working face strike. First, a small number of microfractures occurred in the advancing overlying strata of the working face. As the working face advanced, more microruptures developed in the overburden to the rear of the face. Until the working face advanced to a certain value, the microruptures were concentrated in a specific area. In this area, the microruptures interacted with each other to form microfractures. These microfractures continued to expand and develop into macrofractures. Furthermore, as the working face advanced, these microfractures periodically developed into macrofractures.

In combination with ground pressure observations, the main roof was found to be overhanging after the initial collapse of the immediate roof. Therefore, the weight of the overlying layer was directly transferred to the coal wall through a rock beam formed from the main roof. Part of the broken main roof was pressed against the collapsed gangue, and the working face was protected by the rock beam. When the overhang reached a certain length, the main roof broke along the coal wall under the action of its own weight and the overlying strata load. The main roof collapsed cyclically as the working face advanced; this phenomenon is known as periodic pressure.

Microseismic events monitored using microseismic techniques also exhibit this pattern, as shown in Figure 13. A high incidence of microseismic events occurred approximately every 2 days, with a significant increase in the number of events and energy levels. This indicates an incoming periodic pressure phenomenon when a large number of microseismic events are concentrated. Microfractures expand, penetrate, develop, and eventually form macrofractures. At the same time, this leads to the occurrence of main roof fractures, damage, and falling. The area of concentrated microseismic events was 19.7–24 m above the coal seam according to statistics. In other words, the main roof broke within this range. Thus, the height of the fall zone was determined as 19.7–24 m.

Three stages were identified by analyzing the evolution of the microseismic events during this period. First, few microruptures were generated in the overlying strata at the beginning, known as the fracture budding stage. The number of microseismic events at this stage was small, and the energy was low. As the distance from the advanced working face increased, new fractures were created and expanded on the fractures from the previous stage. The number of microseismic events increased and the energy released increased during this stage, which corresponded

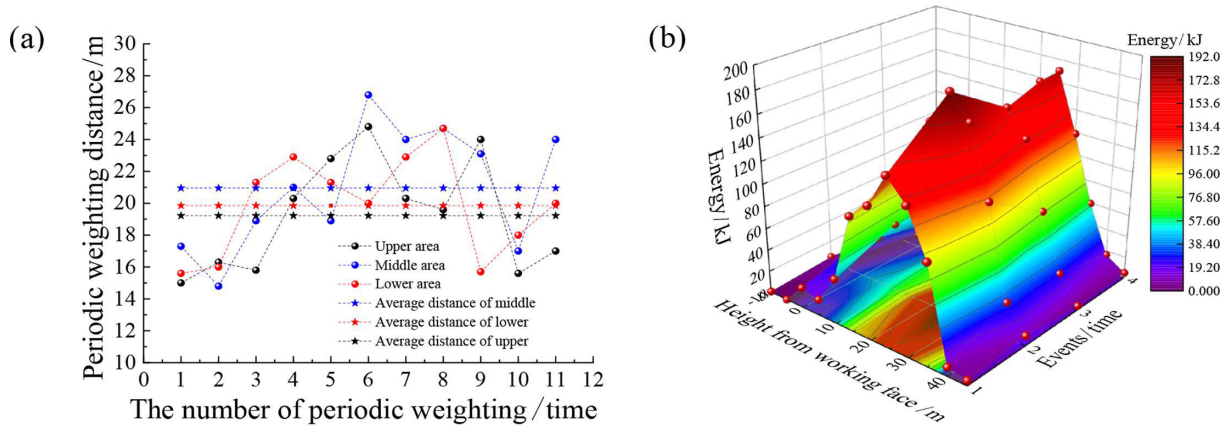

FIGURE 15: Energy distribution characteristics of microseismic events. (a) Average value of the periodic weighting step. (b) Energy distribution of microseismic events during the period of ground pressure.

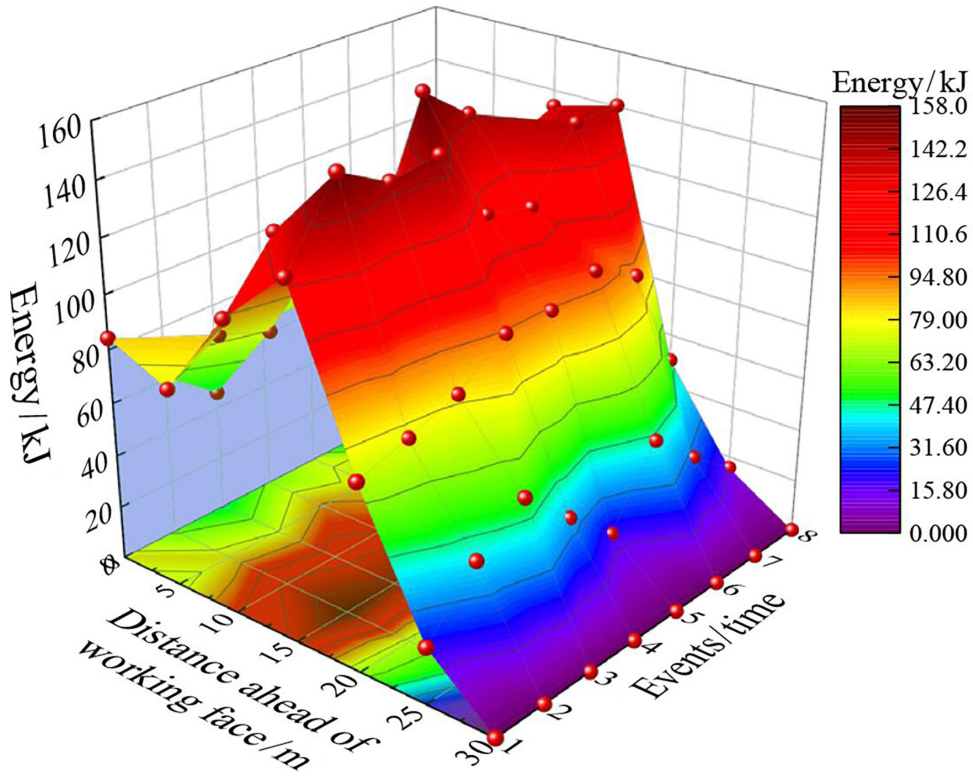

FIGURE 16: Influence area ahead of the working face.

to the fracture development phase. When the advancing distance reached the periodic weighting length, macroscopic fractures formed and strata damage occurred. At this stage, the microseismic distribution was dense, with the greatest energy belonging to the fracture maturation stage. Microseismic events occurred for a brief period of stability and passed through the roof break. The extent of the fissure slowly increased, and the energy of the microseismic events significantly decreased. Once again, microseismic events in the overlying rocks occurred in the budding phase.

6. DISCUSSION

6.1. Determination of Overburden Fracture Zones

It can be found from the key strata breakage and microseismic event evolution laws described previously that fractures in the overlying strata mostly occurred between the subcritical and critical layers. In this area, roof breakage was frequent and the fracture degree was high. The distribution of microseismic events in the overlying rock layer was analyzed against the comprehensive geological column map of the No.S1201-II working face. The specific extent and position of the fracture zone were identified using SFRCP.

This zone was 85–105 m in height and included three coal seams, one layer of fine-grained sandstone, one layer of coarse-grained sandstone, one layer of charcoal mudstone, one layer of mudstone, two layers of fine-grained sandstone, two layers of sandy mudstone, and seven layers of siltstone, as shown in Figure 14.

6.2. Determination and Prediction of Periodic Weighting Step

The number and energy of microseismic events exhibited a cyclical evolution pattern as the working face advanced. The monitoring results for the ground pressure at the working face are shown in Figure 15(a). The periodic weighting steps for the upper, middle, and lower parts of the working face were 15–26, 17–26, and 15.4–24.7, respectively, with an average of 20.5, 21.5, and 20.68 m, respectively. The completed "third" stage of the microseismic events in a periodic weighting step was 19.83 m, which is generally consistent with the on-site mine pressure observation.

Multiple ground pressures occurred during microseismic monitoring. Four of these were analyzed to determine the energy threshold for overburden breakage. The cumulative energy values of the microseismic events during the period of ground pressure in different layers were determined (Figure 15(b)). As shown in the figure, the cumulative energy release from the microseismic events reached a maximum of 1.9×10^5 J 25 m above the coal seam. The lowest cumulative energy was 1.48×10^5 J, with an average of 1.7×10^5 J. The overlying strata broke owing to the ground pressure. Therefore, the minimum value of 1.48×10^5 J of the cumulative energy from the four microseismic events was used as the threshold value to determine whether the main roof was broken.

6.3. Determination and Prediction of the Influence Area Ahead of the Working Face

In total, 2875 microseismic events were selected for counting and analysis. The minimum value of the accumulated energy among the microseismic events was used as the threshold to determine whether the main roof was broken. The maximum accumulated energy of the microseismic events in different areas of the working face exceeded the threshold value of 148 kJ, corresponding to a range of up to 15 m ahead of the working face (Figure 16). The fracture was developed by a large number of microfractures in this area, which led to roof breakage and collapse after mining of the working face. It was easily found that when the accumulated energy was lower than the threshold value in the influence area ahead of the working face, the microseismic events were relatively few and low in energy. Moreover, when the energy was greater than the threshold, the microseismic events were greater in number and high in energy.

7. CONCLUSIONS

In summary, numerical simulations, physical experiments, and engineering practices were combined in a case study. The spatiotemporal evolution laws of the overburden fracture field were revealed based on microseismic-monitoring technology. A method of predicting the working face periodic weighting step and the influence area ahead of the working face was obtained, and the results were as follows:

(1) The working face length increased after roof cutting, which led to an increase in the peak pressure on the side farther away from the goaf. The roof displacement remained essentially unchanged when the roadway was in the digging and cutting stages. However, the roof displacement continued to increase during the sinking and forming stages.

(2) The height of the fall zone before roof cutting was approximately 17.1–19.4 m, which was 4.3–4.8 times the mining height. The maximum heights of fracture zone development on both sides and in the middle of the working face were 103.6–106.4 and 92.4–96.1 m, respectively, corresponding to 25.9–26.6 and 23.1–24.0 times the mining height, respectively. The height of the fall zone after cutting was approximately 18.1 m, which was 4.5 times the mining height. The maximum heights of the fracture zone on both sides and in the middle of the working face were 100.6–105.2 and 91.3–95.2 m, respectively, corresponding to 25.1–26.3 and 22.8–23.8 times the mining height, respectively.

(3) The evolution law of the fracture field was determined quantitatively based on the number and energy of microseismic events using SFRCP. The fully developed fracture area lay 21–85 m above the coal seam and 54–66 m in the direction of the working face inclination. The microseismic events were compared with the comprehensive geological column map of the No.S1201-II working face. The concentration areas of the microruptures were then identified.

(4) Combined with the ground pressure behaviors and overburden-broken characteristics monitored in the field, the fracture budding, development, and maturation phases were divided according to the distribution characteristics of the microseismic events. The idea of using the periodic accumulated microseismic energy value as a criterion for the periodic fracture of the roof and the influence area ahead of the working face was proposed.

Data Availability

The data used to support the findings of this study are available from the corresponding author upon request.

Conflicts of Interest

We have no conflicts of interest to disclose. All authors declare that they have no conflicts of interest.

Funding Statement

This work was supported by National Natural Science Foundation of China (grant number 52204151), China Postdoctoral Science Foundation (grant number 2022MD713796), Excellent Youth Foundation of Shaanxi (grant number 2023-JC-JQ-42), and the Youth Innovation Team of Shaanxi Universities (grant number 2022–23).

Acknowledgments

The authors would also like to thank the anonymous reviewers for their comments and suggestions to improve the manuscript.

References:

[1] Q. Wang, M. He, J. Yang, H. Gao, B. Jiang, and H. Yu, "Study of a no-pillar mining technique with automatically formed gob-side entry retaining for longwall mining in coal mines," *International Journal of Rock Mechanics and Mining Sciences*, vol. 110, pp. 1–8, 2018.

[2] M. C. He, Z. Q. Song, A. Wang, et al, "Theory of longwall mining by using roof cuting shortwall team and 110 method —the third mining science and technology reform," *Coal Science & Technology Magazine*, vol. 1, pp. 1–9, 2017.

[3] Y. Gao, Y. Wang, J. Yang, X. Zhang, and M. He, "Meso- and macroeffects of roof split blasting on the stability of gateroad surroundings in an innovative nonpillar mining method," *Tunnelling and Underground Space Technology*, vol. 90, pp. 99–118, 2019.

[4] J. Yang, M. C. He, and C. Cao, "Design principles and key technologies of gob side entry retaining by roof pre-fracturing," *Tunnelling and Underground Space Technology*, vol. 90, pp. 309–318, 2019.

[5] B. Zhou, J. Xu, M. Zhao, and Q. Zeng, "Stability study on naturally filling body in gob-side entry retaining," *International Journal of Mining Science and Technology*, vol. 22, no. 3, pp. 423–427, 2012.

[6] M. He, W. Gong, J. Wang, et al., "Development of a novel energy-absorbing bolt with extraordinarily large elongation and constant resistance," *International Journal of Rock Mechanics and Mining Sciences*, vol. 67, pp. 29–42, 2014.

[7] Y. L. Tan, F. H. Yu, J. G. Ning, and T. B. Zhao, "Design and construction of entry retaining wall along a gob side under hard roof stratum," *International Journal of Rock Mechanics and Mining Sciences*, vol. 77, pp. 115–121, 2015.

[8] Y. Xu, J. Chen, and J. B. Bai, "Control of floor heaves with steel pile in gob-side entry retaining," *International Journal of Mining Science and Technology*, vol. 26, no. 3, pp. 527–534, 2016.

[9] L. Chen, W. Guo, Y. Jiang, et al., "Experimental study on influence of lithology on directional propagation law of type-I cracks," *Journal of Central South University*, vol. 30, no. 10, pp. 3322–3334, 2023.

[10] W. L. Wang and S. Ma, "Roof cutting gob — side entry retaining in high cutting face under complex stress disturbance," *Coal Engineering*, vol. 52, pp. 33–37, 2020.

[11] Y. Wang, Q. Wang, X. Tian, H. Wang, J. Yang, and M. He, "Stress and deformation evolution characteristics of gob-side entry retained by roof cutting and pressure relief," *Tunnelling and Underground Space Technology*, vol. 123, p. 104419, 2022.

[12] W. Zhang, W. Guo, and Z. Wang, "Influence of lateral pressure on mechanical behavior of different rock types under biaxial compression," *Journal of Central South University*, vol. 29, no. 11, pp. 3695–3705, 2022.

[13] J. P. Li, C. G. Feng, C. B. Zhou, et al, "Study of basic parameters on local grooving top-caving with controlled explosion," *Chinese Journal of Rock Mechanics and Engineering*, vol. 23, pp. 650–656, 2004.

[14] X. M. Sun, X. Liu, G. F. Liang, et al, "Key parameters of gob-side entry retaining formed by roof cut and pressure releasing in thin coal seams," *Chinese Journal of Rock Mechanics and Engineering*, vol. 33, pp. 1449–1456, 2014.

[15] B. X. Huang, J. W. Liu, and Q. Zhang, "The reasonable breaking location of overhanging hard roof for directional hydraulic fracturing to control strong strata behaviors of gob-side entry," *International Journal of Rock Mechanics and Mining Sciences*, vol. 103, pp. 1–11, 2018.

[16] G. F. Zhang, M. C. He, X. G. Yu, et al, "Research on the technique of no-pillar mining with gob-side entry formed by advanced roof caving in the protective seam in Baijiao coal mine," *Journal of Mining & Safety Engineering*, vol. 28, pp. 511–516, 2018.

[17] T. Zhao, P. Zhang, W. Guo, X. Gong, C. Wang, and Y. Chen, "Controlling roof with potential rock burst risk through different pre-crack length: Mechanism and effect research," *Journal of Central South University*, vol. 29, no. 11, pp. 3706–3719, 2022.

[18] GIBWICZ. S. J., "Seismicity induced by mining," *Advance in Geophsics*, vol. 32, pp. 49–80, 1990.

[19] S. Y. Li, X. S. He, S. Q. Zhang, et al, "Progress and the latest achievements in mine earthquake monitoring technology," *Progress in Geophysics*, vol. 19, pp. 853–859, 2004.

[20] S. L. Li, "Discussion on microseismic monitoring technology and its applications to underground projects," *Chinese Journal of Underground Space and Engineering*, vol. 5, pp. 122–128, 2009.

[21] B. R. Chen, X. T. Feng, Q. Q. Fu, et al, "Integration and high precision intelligence microseismic monitoring technology and its application in deep rock engineering," *Rock and Soil Mechanics*, vol. 41, pp. 2422–2431, 2020.

[22] X. Li, D. Chen, J. Fu, S. Liu, and X. Geng, "Construction and application of fuzzy comprehensive evaluation model for rockburst based on microseismic monitoring," *Applied Sciences*, vol. 13, no. 21, p. 12013, 2023.

[23] H. Li, X. Li, J. Fu, et al., "Experimental study on compressive behavior and failure characteristics of imitation steel fiber concrete under uniaxial load," *Construction and Building Materials*, vol. 399, p. 132599, 2023.

[24] H. Li, X. Li, J. Fu, Z. Gao, P. Chen, and Z. Zhang, "Research on acoustic emission multi-parameter characteristics in the failure process of imitation steel fiber reinforced concrete," *Physics of Fluids*, vol. 35, no. 10, 2023.

[25] J. He, L. Dou, S. Gong, J. Li, and Z. Ma, "Rock burst assessment and prediction by dynamic and static stress analysis based on micro-seismic monitoring," *International Journal of Rock Mechanics and Mining Sciences*, vol. 93, pp. 46–53, 2017.

[26] J. A. Vallejos and S. D. McKinnon, "Logistic regression and neural network classification of seismic records," *International Journal of Rock Mechanics and Mining Sciences*, vol. 62, pp. 86–95, 2013.

[27] T.-H. Ma, C.-A. Tang, S.-B. Tang, et al., "Rockburst mechanism and prediction based on microseismic monitoring," *International Journal of Rock Mechanics and Mining Sciences*, vol. 110, pp. 177–188, 2018.

[28] G. Li and C. A. Tang, "A statistical meso-damage mechanical method for modeling trans-scale progressive failure process of rock," *International Journal of Rock Mechanics and Mining Sciences*, vol. 74, pp. 133–150, 2015.

[29] B. S. Hu, Y. P. Wu, Y. Yu, et al, "Numerical study on the dynamic pressure control for self-forming roadways using CHRCT in thin coal seams with thick and hard roofs," *Energy Exploration & Exploitation*, 2024.